



UNIVERSITY OF LEEDS

This is a repository copy of *Shutter-speed dynamic contrast-enhanced MRI: is it fit for purpose?*.

White Rose Research Online URL for this paper:
<http://eprints.whiterose.ac.uk/133188/>

Version: Accepted Version

Article:

Buckley, DL orcid.org/0000-0001-6659-8365 (2019) Shutter-speed dynamic contrast-enhanced MRI: is it fit for purpose? *Magnetic Resonance in Medicine*, 81 (2). pp. 976-988. ISSN 0740-3194

<https://doi.org/10.1002/mrm.27456>

© 2018 International Society for Magnetic Resonance in Medicine. This is the peer reviewed version of the following article: Buckley, DL (2018) Shutter-speed dynamic contrast-enhanced MRI: is it fit for purpose? *Magnetic Resonance in Medicine*, which has been published in final form at <https://doi.org/10.1002/mrm.27456>. This article may be used for non-commercial purposes in accordance with Wiley Terms and Conditions for Use of Self-Archived Versions.

Reuse

Items deposited in White Rose Research Online are protected by copyright, with all rights reserved unless indicated otherwise. They may be downloaded and/or printed for private study, or other acts as permitted by national copyright laws. The publisher or other rights holders may allow further reproduction and re-use of the full text version. This is indicated by the licence information on the White Rose Research Online record for the item.

Takedown

If you consider content in White Rose Research Online to be in breach of UK law, please notify us by emailing eprints@whiterose.ac.uk including the URL of the record and the reason for the withdrawal request.



eprints@whiterose.ac.uk
<https://eprints.whiterose.ac.uk/>

Title: Shutter-speed dynamic contrast-enhanced MRI: is it fit for purpose?

Author: David L. Buckley, Biomedical Imaging, University of Leeds, Leeds LS2 9JT, UK.

Correspondence address:

David L. Buckley

Biomedical imaging, University of Leeds

Level 6, LIGHT Laboratories

Clarendon Way, Leeds LS2 9JT, UK

Email – d.l.buckley@leeds.ac.uk tel. +44 113 343 2017

Word count: 3404 words (not including the Appendices)

Shutter-speed dynamic contrast-enhanced MRI: is it fit for purpose?

Abstract

Purpose: To test the ability of shutter-speed dynamic contrast-enhanced (DCE) MRI to estimate water exchange (WX) using simulations and assess its performance in clinical case studies of malignant and benign breast tumors.

Methods: Data were simulated using a one-compartment tracer kinetic (TK) model combined with a two-pool WX model (2PX) and with a two-compartment TK model. Typical DCE-MRI acquisition parameters were used with both WX-sensitive (8°) and insensitive (25°) flip angles. Clinical data were obtained from patients with malignant and benign breast tumors. Data were fitted using a two-compartment TK model and a one-compartment TK model combined with four WX models: fast exchange limit (FXL), no exchange, 2PX and shutter-speed.

Results: Fits to the one-compartment simulated data were excellent but estimates of WX obtained using the 2PX and shutter-speed models were poor. One-compartment TK model fits to the clinical malignant tumor data were bad except for the shutter-speed model. However, that overestimated TK parameters compared to the best-fit two-compartment TK model which predicted a significant blood volume and leaky capillaries (one tracer compartment is insufficient, two are necessary). All models produced excellent fits to the clinical benign tumor data with little variation between parameter estimates (one tracer compartment is sufficient).

Conclusion: The 2PX and shutter-speed models were unable to estimate WX from the DCE-MRI data. A good fit to malignant tumor data using the shutter-speed model was not explained by WX but the choice of an inappropriate TK model leading to distorted parameter estimates.

Keywords: dynamic contrast-enhanced MRI; tracer kinetics; transcytolemmal water exchange; tumor perfusion; capillary permeability.

Introduction

Quantitative dynamic contrast-enhanced (DCE) imaging experiments are often performed to make estimates of hemodynamic parameters such as the transfer constant (K^{trans}), as well as more specific parameters such as blood flow (F_b), blood volume (v_b), capillary permeability surface-area product (PS) and interstitial volume (v_e) [1]. When these experiments are performed using radiotracers and PET or SPECT, or using an iodinated contrast agent and DCE-CT, we observe the effect of the tracer directly and there's a straightforward relationship linking signal with tracer concentration. With DCE-MRI the relationship is more complicated because we don't 'see' the tracer (typically a gadolinium-based contrast agent) directly but rather measure its effect on water in the local environment. If that water is moving very rapidly through the tissue then water exchange (WX) between tissue compartments can be neglected, we measure a single average tissue longitudinal relaxation rate, R_1 ($1/T_1$), subtract the baseline R_{1_0} and the difference is directly proportional to tissue tracer concentration [2]. If the water moves more slowly between tissue compartments (e.g. between interstitium and cell) and there's a difference between the R_1 of those compartments (which might occur when contrast agent enters the interstitium but not the cell) then we may no longer see a single tissue R_1 but might begin to observe two distinct R_1 components in the tissue and can't perform our simple subtraction. Such a scenario is exploited by shutter-speed DCE-MRI [3]. Here cell-interstitial (transcytolemmal) WX is modelled and quantified alongside the tracer kinetics. And while the shutter-speed model has found application in several studies (e.g. [4,5]), it has been criticized [6], not least because the typical DCE-MRI experiment employs an imaging sequence which is, by design, WX-insensitive [7].

Measurements of WX have been made using MR for a long time [8]. Like DCE-MRI many of these experiments employ contrast agents (typically Mn-based in the past) to reduce the R_1 or transverse relaxation rate (R_2) of water in one compartment. Unlike DCE-MRI, they typically employ high doses of contrast agent and make measurements during a steady-state rather than while the contrast agent concentration is changing. Experiments of this type continue to be performed and can provide important information about WX [9]. For example, experiments on yeast cells [10] employed steady-state contrast agent at a concentration of 9.3 mM, levels only seen in DCE-MRI experiments in the arterial blood at the peak of the first pass of the contrast agent bolus (i.e. for a few seconds). Hence it can be seen that while there's a historical precedent for contrast-enhanced measures of WX, the implementation is very different.

Potential problems with the shutter-speed model have been highlighted previously [6]. The version employed in almost all studies to date, the so-called fast exchange regime allowed (FXR-a) version,

makes an unnecessary simplifying assumption about the relationship between signal intensity (SI) and contrast agent concentration. It assumes that this can be approximated by a single R1 term ($R1_L$; two R1 terms define the parent model, $R1_L$ and $R1_S$, as described in Appendix 1) but this doesn't make the model any easier to use; both models are described by three parameters. This can lead to inaccurate estimates of the model parameters as the apparent WX rate slows down and two distinct R1 components emerge [6]. Moreover, it's apparent that estimates of the WX-related parameter made using the shutter-speed model (τ_i , the intracellular residence time of water) are imprecise [6,11]. Nevertheless, the shutter-speed model has generated considerable interest in the DCE-MRI community not least because it often fits the data better than the standard one-compartment Tofts model [4,12], produces results which may help in the differential diagnosis of breast cancer [5] and yields estimates of an additional parameter, τ_i , which, it has been suggested, may reflect important metabolic characteristics of the cells in the tissue imaged [13].

Given the previously highlighted problems [6], the purpose of this study was twofold. First, to test the shutter-speed model using simulations based upon its parent model to assess its ability to estimate τ_i from typical DCE-MRI studies. In this case the reference application was breast cancer, since this is a field in which the shutter-speed model has generated significant interest [5,14]. Considering the results of the simulations, and by analysis of clinical patient data, a second aim was to try and understand why the shutter-speed model produces apparently promising clinical results when applied to the analysis of breast cancer data.

Methods

Simulations

Data were simulated using arterial input functions (AIF) measured from the descending aorta of the patients described below. Gaps in the tails of the AIF data resulting from the use of an interleaved acquisition were filled by interpolation using a biexponential function leading to continuous AIFs extending over approximately 7 minutes and sampled every 2 s. The SI-time curves were converted to plasma contrast agent concentration-time curves using bookend estimates of blood T1 obtained before contrast agent administration and during the slow wash-out [15], measured hematocrit and an assumed contrast agent relaxivity of $4.2 \text{ s}^{-1} \text{ mM}^{-1}$ [16]. Using these AIFs, two types of breast tumor SI-time curve were simulated. The first was representative of a malignant invasive ductal carcinoma with a rapid early enhancement and subsequent plateau or wash-out. The second was representative of a benign fibroadenoma with a slower initial enhancement that continued to rise

throughout the imaging period. Both types of curve were initially generated using a one-compartment tracer kinetic model [12] combined with a full two-pool (cell and interstitium) WX model (2PX) [6]; the parent of the shutter-speed model. The parameters used to simulate the data were: baseline $T1 = 1282$ ms, $K^{trans} = 0.13, 0.19, 0.03$ & 0.06 min^{-1} , $v_e = 0.26, 0.39, 0.47$ & 0.62 representing a range of malignant tumors and benign fibroadenomas. Three WX regimes were simulated with $\tau_i = 0.0001, 1000$ & 0.5 s to approximate the fast exchange limit (FXL), the no-exchange limit (NXL) and an intermediate exchange (IX) rate, respectively. As a result of the findings of the clinical case studies (below), a further set of simulations was performed using a two-compartment tracer kinetic model [1] to better mimic the uptake seen by the invasive ductal carcinomas (parameters used - $F_b = 0.28$ & 0.50 $\text{ml}\cdot\text{min}^{-1}\cdot\text{ml}^{-1}$, $v_b = 0.13$ & 0.27 , $PS = 0.08$ & 0.16 $\text{ml}\cdot\text{min}^{-1}\cdot\text{ml}^{-1}$, $v_e = 0.32$); WX was simulated at the FXL only. The sequence parameters used for the case studies (below) were similarly employed for the simulations ($TR = 2.37$ ms and flip angle = 25°). These data could be described as exchange-minimized (due to the short TR and high flip angle [7]), so to increase WX sensitivity all of the above simulations were repeated using a WX optimized flip angle of 8° [17] and, to add further variability to the data, each curve was simulated using AIFs taken from two different patients. Thus, a total of 128 noiseless and well-sampled data sets were generated.

These data sets were fitted using four different one-compartment tracer kinetic models (table 1). As previously [6], the data were fitted using an FXL assumption for WX (the standard approach to fitting DCE-MRI data) and an NXL assumption, each producing estimates of K^{trans} and v_e . They were also fitted using the shutter-speed model and the 2PX model each producing estimates of K^{trans} , v_e and τ_i . The data simulated using the two-compartment tracer kinetic model were additionally fitted using the two-compartment model and details of each of the models are provided in Appendix 1. 95% confidence intervals were estimated on each fit parameter and fit quality was compared between models using the corrected Akaike information criterion (cAIC) that takes account of the number of fit parameters as well as sum-of-square residuals [18].

Clinical Case Studies

Data were acquired from three patients undergoing DCE-MRI before they started a course of neoadjuvant chemotherapy for primary breast cancer. The patients, who were part of a larger study that received approval from a local research ethics committee, provided written informed consent. The imaging protocol, performed at 1.5 T (Siemens Aera; Siemens, Erlangen, Germany), included a baseline T1 measurement (multi-shot 3D inversion recovery-prepared turboFLASH acquisitions at TI

100, 600, 1200 and 2800 ms), an interleaved high spatial resolution/high temporal resolution DCE-MRI acquisition [19] following the administration of 0.1 mmol.kg⁻¹ Gd-DOTA (Dotarem; Guerbet Laboratories, Aulnays Sous Bois, France). The subsequently analyzed high temporal resolution DCE-MRI data were acquired every 2 s using a 3D FLASH sequence (TR/TE 2.37/0.73 ms, flip angle of 25°, CAIPIRINHA parallel imaging factor 2 x 2). After approximately 7 mins a second bookend T1 measurement was obtained [15]. AIFs and breast tumor SI-time curves were extracted from each of the patient studies. Three tumors (one from each patient) were malignant invasive ductal carcinomas and two (from two of the three patients) were benign fibroadenomas (all confirmed by histopathological analysis of diagnostic biopsies).

Results

Simulations

The simulated data broadly reflected the SI-time curve shape seen in the clinical data (Figs. 1 & 2). Fits to the one-compartment/2PX simulated data by all one-compartment models were visibly excellent but parameter estimates were not always accurate. Example parameter estimates are presented in Appendix 2 (tables A1 & A2). Data simulated at the FXL and NXL for both flip angles were best fitted by the FXL and NXL models, respectively. While there was little difference in the results obtained by fitting with other models to the data simulated with a 25° flip angle, when fitted to the 8° flip angle data the results were more variable. The NXL model fits to the 8° flip angle FXL simulated data produced inaccurate parameter estimates (it overestimated both K^{trans} and v_e). Correspondingly, the FXL model fits to the 8° flip angle NXL simulated data underestimated both K^{trans} and v_e . Data simulated at an IX rate with a 25° flip angle were fitted well by all models though estimates of τ_i were poor with the 2PX and shutter-speed models. Fits to the 8° flip angle IX data using the 2PX model gave variable results which depended upon the starting guesses provided (e.g. it could produce an ideal solution from excellent starting guess for τ_i). The shutter-speed model fits were less variable, but these produced inaccurate estimates of τ_i . Both the FXL and NXL model fits to the 8° flip angle IX data resulted in inaccurate estimates of K^{trans} and v_e (underestimates and overestimates, respectively). When the shutter-speed model was fitted to any of the simulated fibroadenoma data v_e was systematically overestimated. Despite the WX sensitivity of the 8° flip angle acquisition and the absence of noise in the data, τ_i parameter estimates were poor for almost all simulated data sets using either 2PX or shutter-speed models.

The FXL, NXL and 2PX one-compartment model fits to data simulated using the two-compartment model were poor, with systematic misfits highlighted by structured residuals, and the shutter-speed model fitted better every time. However, in every case, the shutter-speed model overestimated K^{trans} and v_e and the two-compartment model produced the best fits of all (see, for example, Fig. 3).

Clinical Case Studies

FXL and NXL model fits to the clinical malignant tumor data were poor (an example of each is shown in Fig. 4a, b) and this wasn't improved by fitting with the 2PX model (Fig. 4c). Conversely, the shutter-speed model fits were far better (Fig. 4d) and produced much higher estimates of K^{trans} and v_e than those provided by the other three one-compartment models (K^{trans} was 53%, 60% & 80% higher than the FXL estimates & v_e was 130%, 31% & 146% higher than the FXL estimates). These results reflect the findings reported by others using the shutter-speed model, i.e. the reported malignant specificity of ΔK^{trans} , the difference between the shutter-speed estimate and the FXL estimate of K^{trans} [5,14]. Nevertheless, the best fits of all were obtained using the two-compartment model (Fig. 4e). The parameter estimates suggesting that the malignant tumors had leaky capillaries ($PS = 0.08, 0.06 \text{ \& } 0.16 \text{ ml}\cdot\text{min}^{-1}\cdot(\text{ml tissue})^{-1}$, first-pass extraction fractions of 32%, 22% & 35%) and large blood volumes (27%, 23% & 14%). From these data K^{trans} was calculated to be 0.05, 0.05 & 0.10 min^{-1} and v_e , 0.48, 0.26 & 0.41.

FXL and NXL model fits to the clinical fibroadenoma data were very good (the FXL model fit had marginally lower cAIC in both cases and was therefore preferred over the other fits, Fig. 5a, b). The fits did not improve by fitting with the 2PX or shutter-speed models (Fig. 5c, d) and the shutter-speed model generated an increased estimate of v_e (27% & 112% higher than the FXL estimate). Again, this result reflects the findings reported previously with very small ΔK^{trans} in benign lesions [5,14]. The two-compartment model produced fits that were very similar to the other models (Fig. 5e) and parameter estimates suggested that the fibroadenomas had leaky capillaries ($PS = 0.43 \text{ \& } 0.20 \text{ ml}\cdot\text{min}^{-1}\cdot(\text{ml tissue})^{-1}$, first-pass extraction fractions of 86% & 83%) and small blood volumes (4% & 2%). Using these estimates K^{trans} was calculated to be 0.06 & 0.03 min^{-1} and v_e , 0.62 & 0.45. However, these two-compartment model parameter estimates were very imprecise (see Fig. 5), the fits were over-parameterized and a one-compartment model was sufficient to describe the tracer kinetics in both fibroadenomas [20].

Discussion

The shutter-speed model has been regularly promoted to the MR community for over 15 years and has attracted significant interest from users of DCE-MRI. What has been lacking is validation of the model and its applications. It is clear from these simulations (and previous experimental work [6]) that while models incorporating WX - the 2PX and shutter-speed models - can provide acceptable estimates of K^{trans} , estimation of τ_i is not viable. Even when noiseless data are simulated with exchange-sensitive sequences (i.e. in this study an 8° flip angle, [17]), the models don't produce accurate and reliable estimates of τ_i . The shutter-speed model is ill-posed with significant correlation between parameters [6]. If this is the case with 'ideal' data (noiseless, high sampling frequency, simulated using the parent model), it raises serious concerns about their ability to provide meaningful parameter estimates from noisy, and often under-sampled, clinical data. Given these negative findings, how has the shutter-speed model produced apparently successful results in the differential diagnosis of breast cancer [5]?

This question can be addressed by examining the findings from the two-compartment simulated data and clinical case studies. The apparently excellent fits to the malignant tumor data produced by the shutter-speed model (e.g. Figs. 3d & 4d) compared to the bad FXL fits (Figs. 3a & 4a) are not a reflection of unusual WX in the tumor cells (e.g. that might represent abnormal metabolism). If it were, then the parent WX model, the 2PX model, would surely reflect this too. The FXL, NXL and 2PX models are unable to reproduce the 'flattened' SI-time response of the malignant tumor (Fig. 4) because their one-compartment tracer kinetic model restricts the SI-time response to a limited range of curvature. The shutter-speed model achieves a better fit through its artificially enhanced non-linear SI-contrast agent concentration relationship [6,21].

Fig. 6a shows calibration curves relating SI to interstitial contrast agent concentration for the imaging sequence used to obtain these data, $v_e = 0.39$ (obtained from the NXL model fit to the first malignant tumor) and a literature value for τ_i of 400 ms [21]. The shutter-speed model calibration curve is more non-linear than the response of the other three models, it breaks out beyond the WX limits that should define its range of influence [6]. The red (FXL) and blue (NXL) lines represent the extremes of WX and any 'correct' model must predict a response somewhere between these two. However, when we use the parameter estimates obtained from the shutter-speed model fit to plot a calibration curve ($v_e = 0.86$, $\tau_i = 714$ ms; Fig. 6b) we can see that the shutter-speed model non-linearity has become even more pronounced. The model parameters have taken on new, hyper-physiologic, values to achieve the required flattening of the SI-time curve and a good fit to the malignant tumor data. They no longer reflect a scenario caused by WX (if they did, the 2PX model

would do the same), they simply distort as a 'means to an end' - to best match to the data. The shutter-speed model is distorting to fit to data that aren't appropriately described by a one-compartment tracer kinetic model. As confirmed by the fit to the two-compartment model (the best fit; the lowest cAIC), the delivery and distribution of the contrast agent in the malignant tumor requires two compartments to properly reflect its kinetics. The contrast agent is distributing in two tissue pools with substantial volumes; the blood plasma occupying 16% of the tissue water pool, and interstitium occupying 32%.

The counterpart to the results seen in the malignant tumors are those seen in the benign fibroadenomas (e.g. Fig. 5). Here, one compartment is sufficient to describe the tracer kinetics. Once the extraction fraction is high enough, it becomes difficult to differentiate contrast agent in the blood from contrast agent in the interstitium [20], a situation similarly seen in the heart at rest where a one-compartment model is sufficient to describe myocardial blood flow [22]. Like the 25° flip angle simulations, with little WX sensitivity in the acquisition, the 2PX, shutter-speed, FXL and NXL models all produce very similar estimates of K^{trans} and all fit the data very well (though the shutter-speed model still overestimates v_e). Here, ΔK^{trans} is small, but this has nothing to do with WX, it's all about tracer kinetics. The FXL model, described by only two parameters, produces a good fit and no additional parameters are necessary (whether they describe WX or tracer kinetics) and statistical arguments favor the simplest model (in this case FXL).

Study Limitations

The simulation study may be regarded as error-free and though limited in scope, it only assesses two types of SI-time course, the data are typical of those seen in DCE-MRI of the breast [5]. Conversely, the clinical case studies have several limitations. The analysis requires knowledge of the applied flip angle and this will be influenced by B1 inhomogeneity. This is at least partly addressed using bookend T1 measurements [15]. The AIF is measured a long way from the breast (at the descending aorta). This is a pragmatic choice given the difficulty in measuring an AIF in local, smaller arteries and benefits from the avoidance of partial volume and inflow artefacts [19]. Nevertheless, it is inevitable that some dispersion will occur between the point of measurement and arrival at the breast tumor and this will propagate as a (small) error in the parameter estimates [1]. Furthermore, the acquisition sequence has a finite TE and T2* of the blood at the peak of the AIF is likely to be very short introducing some underestimation of the peak contrast agent concentration. WX is not limited to the cell and interstitium, blood-interstitial (transendothelial) WX is very likely to influence the measured SI from the malignant tumor and this will need to be addressed in future studies [23]. We

have included patient-specific measures of the large vessel hematocrit, but modelling results will depend somewhat on the microvascular hematocrit, which is unknown.

Conclusions

The simulations show that both the shutter-speed and 2PX models are unable to estimate WX (τ_i) from noise-free simulated DCE-MRI data even when the flip angle is reduced to enhance WX sensitivity [17] confirming previous experimental findings [6]. Furthermore, the specificity of shutter-speed DCE-MRI for the differential diagnosis of primary breast tumors [5] looks most likely to reflect an inappropriate choice of tracer kinetic model for analyzing the malignant tumor data; the one-compartment tracer kinetic model is under-parameterized and should not be used to fit those data. The shutter-speed model tries to overcome one problem by creating another - confusing neglected vascular signal for WX. DCE-MRI is designed to measure tracer kinetics, the attempt to combine WX estimates with tracer kinetic estimates using shutter-speed DCE-MRI results in bad estimates of both. The shutter-speed model is not providing meaningful estimates of τ_i and in many cases (e.g. when ΔK^{trans} is significant) it is also producing systematic errors in its estimates of K^{trans} and v_e .

Acknowledgments

This paper was developed from an educational presentation given at the 25th Annual Meeting of the ISMRM in Honolulu, April 2017. The data were collected with support from Breast Cancer Now (award 2014MayPR241) and were analyzed with help from Leonidas Georgiou. Greg Stanisz and Steven Sourbron provided helpful comments on an early draft of the manuscript.

References

1. Sourbron SP, Buckley DL. Tracer kinetic modelling in MRI: estimating perfusion and capillary permeability. *Phys Med Biol* 2012;57(2):R1-R33.
2. Donahue KM, Burstein D, Manning WJ, Gray ML. Studies of Gd-DTPA relaxivity and proton-exchange rates in tissue. *Magn Reson Med* 1994;32:66-76.
3. Yankeelov TE, Rooney WD, Li X, Springer CS. Variation of the relaxographic "shutter-speed" for transcytolemmal water exchange affects the CR bolus-tracking curve shape. *Magn Reson Med* 2003;50(6):1151-1169.

4. Kim S, Quon H, Loevner LA, Rosen MA, Dougherty L, Kilger AM, Glickson JD, Poptani H. Transcytolemmal water exchange in pharmacokinetic analysis of dynamic contrast-enhanced MRI data in squamous cell carcinoma of the head and neck. *J Magn Reson Imaging* 2007;26(6):1607-1617.
5. Huang W, Tudorica LA, Li X, Thakur SB, Chen Y, Morris EA, Tagge IJ, Korenblit ME, Rooney WD, Koutcher JA, Springer CS, Jr. Discrimination of Benign and Malignant Breast Lesions by Using Shutter-Speed Dynamic Contrast-enhanced MR Imaging. *Radiology* 2011;261(2):394-403.
6. Buckley DL, Kershaw LE, Stanisiz GJ. Cellular-interstitial water exchange and its effect on the determination of contrast agent concentration in vivo: dynamic contrast-enhanced MRI of human internal obturator muscle. *Magn Reson Med* 2008;60(5):1011-1019.
7. Donahue KM, Weisskoff RM, Chesler DA, Kwong KK, Bogdanov AA, Jr., Mandeville JB, Rosen BR. Improving MR quantification of regional blood volume with intravascular T1 contrast agents: accuracy, precision, and water exchange. *Magn Reson Med* 1996;36:858-867.
8. Herbst MD, Goldstein JH. A review of water diffusion measurement by NMR in human red blood cells. *Am J Physiol* 1989;256(5 Pt 1):C1097-1104.
9. Bailey C, Moosvi F, Stanisiz GJ. Mapping water exchange rates in rat tumor xenografts using the late-stage uptake following bolus injections of contrast agent. *Magn Reson Med* 2014;71(5):1874-1887.
10. Zhang Y, Poirier-Quinot M, Springer CS, Jr., Balschi JA. Active trans-plasma membrane water cycling in yeast is revealed by NMR. *Biophys J* 2011;101(11):2833-2842.
11. Zhang J, Kim S. Uncertainty in MR tracer kinetic parameters and water exchange rates estimated from T1-weighted dynamic contrast enhanced MRI. *Magn Reson Med* 2014;72(2):534-545.
12. Tofts PS, Brix G, Buckley DL, Evelhoch JL, Henderson E, Knopp MV, Larsson HB, Lee TY, Mayr NA, Parker GJ, Port RE, Taylor J, Weisskoff RM. Estimating kinetic parameters from dynamic contrast-enhanced T1-weighted MRI of a diffusable tracer: Standardized quantities and symbols. *J Magn Reson Imaging* 1999;10(3):223-232.
13. Springer CS, Jr., Li X, Tudorica LA, Oh KY, Roy N, Chui SY, Naik AM, Holtorf ML, Afzal A, Rooney WD, Huang W. Intratumor mapping of intracellular water lifetime: metabolic images of breast cancer? *NMR Biomed* 2014;27(7):760-773.
14. Huang W, Li X, Morris EA, Tudorica LA, Seshan VE, Rooney WD, Tagge I, Wang Y, Xu J, Springer CS. The magnetic resonance shutter speed discriminates vascular properties of malignant and benign breast tumors in vivo. *Proc Natl Acad Sci U S A* 2008;105(46):17943-17948.
15. Cron GO, Santyr G, Kelcz F. Accurate and rapid quantitative dynamic contrast-enhanced breast MR imaging using spoiled gradient-recalled echoes and bookend T-1 measurements. *Magn Reson Med* 1999;42(4):746-753.
16. Rohrer M, Bauer H, Mintorovitch J, Requardt M, Weinmann HJ. Comparison of magnetic properties of MRI contrast media solutions at different magnetic field strengths. *Invest Radiol* 2005;40(11):715-724.
17. Li X, Huang W, Rooney WD. Signal-to-noise ratio, contrast-to-noise ratio and pharmacokinetic modeling considerations in dynamic contrast-enhanced magnetic resonance imaging. *Magn Reson Imaging* 2012;30(9):1313-1322.
18. Brix G, Zwick S, Kiessling F, Griebel J. Pharmacokinetic analysis of tissue microcirculation using nested models: multimodel inference and parameter identifiability. *Med Phys* 2009;36(7):2923-2933.
19. Georgiou L, Sharma N, Broadbent DA, Wilson DJ, Dall BJ, Gangi A, Buckley DL. Estimating breast tumor blood flow during neoadjuvant chemotherapy using interleaved high temporal and high spatial resolution MRI. *Magn Reson Med* 2018;79(1):317-326.

20. Sourbron SP, Buckley DL. On the scope and interpretation of the Tofts models for DCE-MRI. *Magn Reson Med* 2011;66(3):735-745.
21. Li X, Huang W, Morris EA, Tudorica LA, Seshan VE, Rooney WD, Tagge I, Wang Y, Xu J, Springer CS, Jr. Dynamic NMR effects in breast cancer dynamic-contrast-enhanced MRI. *Proc Natl Acad Sci U S A* 2008;105(46):17937-17942.
22. Broadbent DA, Biglands JD, Larget A, Sourbron SP, Radjenovic A, Greenwood JP, Plein S, Buckley DL. Myocardial blood flow at rest and stress measured with dynamic contrast-enhanced MRI: comparison of a distributed parameter model with a Fermi function model. *Magn Reson Med* 2013;70(6):1591-1597.
23. Bains LJ, McGrath DM, Naish JH, Cheung S, Watson Y, Taylor MB, Logue JP, Parker GJ, Waterton JC, Buckley DL. Tracer kinetic analysis of dynamic contrast-enhanced MRI and CT bladder cancer data: A preliminary comparison to assess the magnitude of water exchange effects. *Magn Reson Med* 2010;64(2):595-603.

Figure captions.

Fig. 1 – SI-time curves acquired from (a) the descending aorta of three different patients, (b) three malignant tumors (blue) and two benign fibroadenoma (red). Across the two plots the same symbols refer to data acquired from the same patients. The variable gap between the first set of baseline data and those acquired as the contrast agent arrives allows time for the acquisition of baseline high spatial resolution data and preparation of the patient for the injection.

Fig. 2 - Simulated malignant (a & c) and benign data (b) using flip angles of 25° (blue) and 8° (red). Each flip angle was used to simulate data using a one-compartment tracer kinetic model with WX at the FXL, IX rate and NXL (a, b - top to bottom in each group, respectively). The data in (c) were simulated using a two-compartment tracer kinetic model and WX at the FXL.

Fig. 3 - Model fits (red continuous lines) to one example simulated malignant tumor data set with WX at the FXL (blue circles). (a) FXL, (b) NXL, (c) 2PX, (d) shutter-speed and (e) two-compartment model (which produced parameter estimates exactly matching the simulation: $F_b = 0.50 \pm 0.00$ ml.min⁻¹.ml⁻¹, $v_b = 0.27 \pm 0.00$, $PS = 0.16 \pm 0.00$ ml.min⁻¹.ml⁻¹, $v_e = 0.32 \pm 0.00$). Each fit is accompanied by its parameter estimates, cAIC and (below) a plot of the fit residuals (red circles).

Fig. 4 - Model fits (red continuous lines) to clinical malignant tumor data from one example patient (blue circles). (a) FXL, (b) NXL, (c) 2PX, (d) shutter-speed and (e) two-compartment model (which produced the following parameter estimates: $F_b = 0.28 \pm 0.01$ ml.min⁻¹.ml⁻¹, $v_b = 0.27 \pm 0.03$, $PS = 0.08 \pm 0.01$ ml.min⁻¹.ml⁻¹, $v_e = 0.32 \pm 0.03$). Each fit is accompanied by its parameter estimates, cAIC and (below) a plot of the fit residuals (red circles).

Fig. 5 - Model fits (red continuous lines) to fibroadenoma clinical data from one example patient (blue circles). (a) FXL, (b) NXL, (c) 2PX, (d) shutter-speed and (e) two-compartment model (which produced the following parameter estimates: $F_b = 0.11 \pm 0.06$ ml.min⁻¹.ml⁻¹, $v_b = 0.04 \pm 0.30$, $PS = 0.43 \pm 1.34$ ml.min⁻¹.ml⁻¹, $v_e = 0.59 \pm 0.18$). Each fit is accompanied by its parameter estimates, cAIC and (below) a plot of the fit residuals (red circles).

Fig. 6 – Calibration curves relating measured SI to interstitial concentration of contrast agent ([Gd]) using the sequence employed in this study (TR = 2.37 ms, flip angle = 25°, left column and 8°, right column) and a baseline T1 of 1282 ms. The calibration curves largely overlap for the FXL, NXL and 2PX models at 25°. The mismatch between the shutter-speed calibration curves and those of the 2PX can be explained by the missing R1_s component that is additionally shown in these plots. (a) malignant tumor calibration curves calculated with a v_e of 0.39 and τ_i of 400 ms, (b) malignant tumor with v_e of 0.86 and τ_i of 714 ms.

| <i>model</i> | <i>tracer kinetics</i> | <i>R1 components vs [Gd]</i> | <i>parameters estimated</i> |
|---------------------|------------------------|------------------------------|-----------------------------|
| FXL | 1-compartment | 1 – linear | K^{trans}, v_e |
| NXL | | 2 – 1 linear & 1 constant | K^{trans}, v_e |
| 2PX | | 2 – non-linear | K^{trans}, v_e, τ_i |
| shutter-speed | | 1 – non-linear | K^{trans}, v_e, τ_i |
| 2-compartment (FXL) | 2-compartments | 1 – linear | F_b, v_b, PS, v_e |

Table 1 – summary of the models used to fit the DCE data. The models have 1 or 2 compartments to describe tracer kinetics and either 1 or 2 R1 components that may increase linearly with contrast agent concentration ([Gd]) or non-linearly depending upon the WX regime. They produce estimates of between 2 and 4 parameters. Further details are provided in Appendix 1.

Appendix 1 – Theory (adapted from [6])

The 2PX model assumes the tumor contains only two water compartments, intracellular and interstitial water and the subscripts i and e to refer to intracellular and interstitial (extravascular extracellular) water, respectively. These compartments have fractional pool sizes of $(1 - v_e)$ and v_e and inherent longitudinal relaxation rates of $R1_i$ and $R1_e$, respectively. Cellular-interstitial water exchange connects these compartments and the rate is described in terms of the mean residence time of water inside (τ_i) and outside (τ_e) the cells; by conservation of mass, $\tau_e = v_e \cdot \tau_i / (1 - v_e)$.

Longitudinal relaxation of the system is modified by the addition of contrast agent to the interstitial space. This system can be described using a two-pool exchange formalism and the solution has a biexponential form with the T1 relaxation of the system described by two rate constants, $R1_s$ and $R1_L$ and their respective fractional apparent populations, a_s and a_L where $a_s + a_L = 1$:

$$R1_L = \frac{1}{2} \left[R1_i + R1_e + r_1 [Gd] + \frac{1}{\tau_i} + \frac{1}{\tau_e} \right] - \frac{1}{2} \left\{ \left[R1_i - R1_e - r_1 [Gd] + \frac{1}{\tau_i} - \frac{1}{\tau_e} \right]^2 + \frac{4}{\tau_i \tau_e} \right\}^{1/2} \quad [A1]$$

$$R1_s = \frac{1}{2} \left[R1_i + R1_e + r_1 [Gd] + \frac{1}{\tau_i} + \frac{1}{\tau_e} \right] + \frac{1}{2} \left\{ \left[R1_i - R1_e - r_1 [Gd] + \frac{1}{\tau_i} - \frac{1}{\tau_e} \right]^2 + \frac{4}{\tau_i \tau_e} \right\}^{1/2} \quad [A2]$$

$$a_s = \frac{1}{2} - \frac{1}{2} \left(\frac{\left[(R1_i - R1_e - r_1 [Gd]) \cdot (2v_e - 1) + \frac{1}{\tau_i} + \frac{1}{\tau_e} \right]}{\left\{ \left[R1_i - R1_e - r_1 [Gd] + \frac{1}{\tau_i} - \frac{1}{\tau_e} \right]^2 + \frac{4}{\tau_i \tau_e} \right\}^{1/2}} \right) \quad [A3]$$

where $[Gd]$ is the concentration of contrast agent in the interstitial space. These equations contain 3 unknowns $[Gd]$, τ_i and v_e since we assumed that $R1_e = R1_i = R1_0$, the longitudinal relaxation rate of

the tumor measured prior to administration of contrast agent. Three different WX approximations were considered. In the FXL the system (described using Eqns. A1 to A3) is reduced to a single longitudinal relaxation rate, R_1 :

$$R_1 = v_e \cdot (r_1[\text{Gd}] + R_{1e}) + (1 - v_e) \cdot R_{1i} \quad [\text{A4}]$$

In the NXL, Eqns. A1 to A3 are reduced to:

$$R_{1L} = R_{1i} \quad [\text{A5}]$$

$$R_{1S} = R_{1e} + r_1 \cdot [\text{Gd}]$$

$$a_S = v_e$$

$$a_L = 1 - v_e$$

In both approximations (FXL and NXL) there are 2 unknowns, $[\text{Gd}]$ and v_e . In the third approximation, the shutter-speed model, the longitudinal relaxation of the system is described by single exponential rate constant, R_{1L} (\equiv Eqn. A1):

$$R_{1L} = \frac{1}{2} \left[R_{1i} + R_{1e} + r_1 [\text{Gd}] + \frac{1}{\tau_i} + \frac{1}{\tau_e} \right] - \frac{1}{2} \left\{ \left[R_{1i} - R_{1e} - r_1 [\text{Gd}] + \frac{1}{\tau_i} - \frac{1}{\tau_e} \right]^2 + \frac{4}{\tau_i \tau_e} \right\}^{1/2} \quad [\text{A6}]$$

Although in an algebraic sense the SS model differs from the full 2-pool model, it contains the same 3 unknowns, $[Gd]$, τ_i and v_e .

Tracer kinetic analysis is used to estimate $[Gd]$ as a function of time. For the one-compartment models, $[Gd]$ is modelled as a convolution of the measured AIF with a single exponential function:

$$[Gd] = \frac{K^{trans}}{v_e} \cdot C_p(t) * \exp\left(\frac{-K^{trans}}{v_e} t\right) \quad [A7]$$

where * represents a convolution and $C_p(t)$ is the AIF measured in the plasma (i.e. the AIF divided by (1-Hct)). For the two-compartment model, the AIF is convolved with a biexponential function:

$$[Gd] = \frac{F_p}{(v_e + v_p)} \cdot C_p(t) * [A \cdot \exp(-\alpha \cdot t) + (1 - A) \cdot \exp(-\beta \cdot t)] \quad [A8]$$

where the tracer kinetic parameters can be calculated from the fit parameters (F_p , A , α and β) using the expressions: $v_p = F_p / (A(\alpha - \beta) + \beta)$; $PS = v_p(\alpha + \beta - v_p \cdot \alpha \cdot \beta / F_p) - F_p$; $v_e = PS \cdot F_p / (v_p \cdot \alpha \cdot \beta)$.

Here F_p and v_p are blood plasma flow and volume ($= F_b \cdot (1-Hct)$ and $v_b \cdot (1-Hct)$), respectively.

Thus, by combining Eqn A7 with Eqns A1, A2 & A3 the solution to the 2PX model has 3 unknowns, K^{trans} , v_e and τ_i . The shutter-speed model is solved using a combination of Eqns A7 and A6 with the 3 unknowns, K^{trans} , v_e and τ_i . Eqns A7 and A5 and Eqns A7 and A4 combine to solve the NXL and FXL

models, respectively. Each of these solutions contains 2 unknowns, K^{trans} and v_e . Eqns A8 and A4 combine to solve the FXL model when used with the two-compartment tracer kinetic model and measured Hct providing estimates of F_b , PS, v_b and v_e .

To compare the output of the models with the data acquired in our experiments we needed to substitute the simulated relaxation rates of the models into equations describing the signal obtained using our imaging sequence. In the case of the FXL and shutter-speed models the resultant single component R1 is substituted directly into:

$$S = S_0 \frac{\sin(\alpha)[1 - \exp(-TR.R1)]}{[1 - \cos(\alpha)\exp(-TR.R1)]} \quad [A8]$$

where S_0 is the signal that would be obtained using an infinite repetition time, TR, and a 90° flip angle and α is the actual flip angle used. The S_0 term incorporates the effects of T_2^* decay (that is assumed to vary negligibly at short echo times), scaling factors and other sequence settings that may confound signal intensity comparisons. The NXL and 2PX models have biexponential solutions and the $R1_s$ and $R1_L$ components are substituted into:

$$S = S_0 \left\{ a_s \frac{\sin(\alpha)[1 - \exp(-TR.R1_s)]}{[1 - \cos(\alpha)\exp(-TR.R1_s)]} + a_L \frac{\sin(\alpha)[1 - \exp(-TR.R1_L)]}{[1 - \cos(\alpha)\exp(-TR.R1_L)]} \right\} \quad [A9]$$

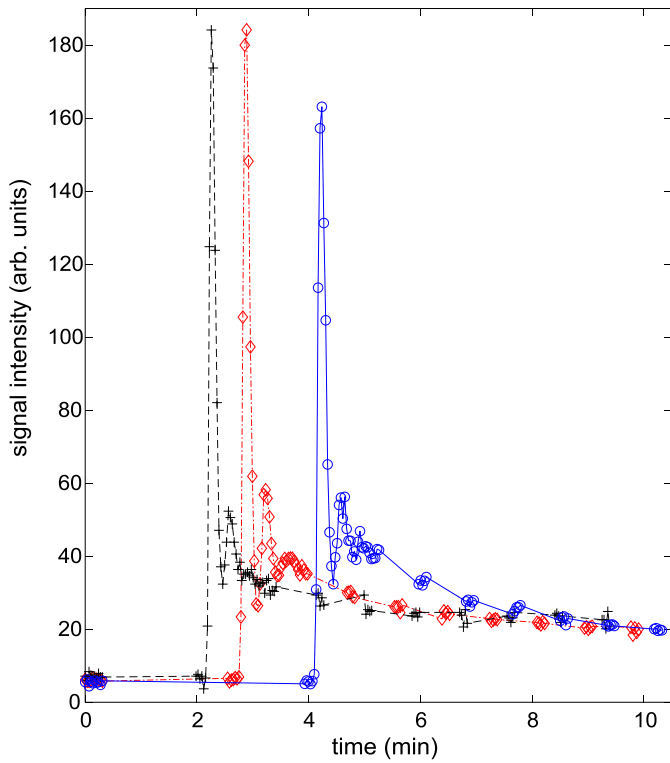
Appendix 2 – Parameter estimates obtained from fits to some example simulated data

Table A1 – Example results of fits to simulated malignant tumor data. Parameter values used to simulate the data are shown and below them parameter estimate \pm 95% confidence intervals from each model fit are shown. The best fit (according to the cAIC) is highlighted in bold.

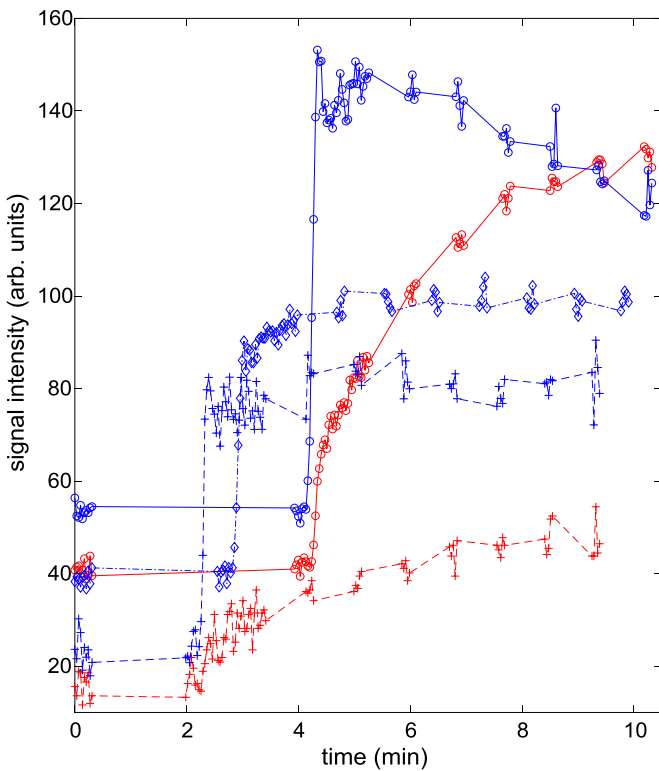
| | $K^{trans} / \mu \times 10^{-3} \text{ min}^{-1}$ | v_e | τ_1 / s | cAIC |
|----------------------|---|-------------------------------------|-------------------------------------|---------------|
| FXL (25°) simulated | 130.0 | 0.390 | 0.0001 | |
| FXL fit | 130.0 \pm 0.000 | 0.390 \pm 0.000 | N/A | -8.50 |
| NXL fit | 136.6 \pm 0.226 | 0.417 \pm 0.001 | N/A | -4.83 |
| 2PX fit | 135.0 \pm 0.627 | 0.411 \pm 0.003 | 0.171 \pm 0.084 | -4.98 |
| shutter-speed | 134.2 \pm 0.507 | 0.407 \pm 0.002 | 0.035 \pm 0.004 | -5.08 |
| NXL (25°) simulated | 130.0 | 0.390 | 1000 | |
| FXL fit | 123.3 \pm 0.197 | 0.363 \pm 0.000 | N/A | -4.83 |
| NXL fit | 130.0 \pm 0.000 | 0.390 \pm 0.000 | N/A | -10.54 |
| 2PX fit | 128.6 \pm 0.168 | 0.384 \pm 0.001 | 0.218 \pm 0.031 | -5.76 |
| shutter-speed | 133.6 \pm 0.473 | 0.406 \pm 0.002 | 0.089 \pm 0.004 | -5.14 |
| IX (25°) simulated | 130.0 | 0.390 | 0.5 | |
| FXL fit | 124.0 \pm 0.178 | 0.366 \pm 0.000 | N/A | -4.89 |
| NXL fit | 130.7 \pm 0.022 | 0.393 \pm 0.000 | N/A | -6.18 |
| 2PX fit | 129.4 \pm 0.084 | 0.388 \pm 0.000 | 0.234 \pm 0.018 | -6.16 |
| shutter-speed | 134.1 \pm 0.526 | 0.408 \pm 0.002 | 0.087 \pm 0.004 | -5.07 |
| FXL (8°) simulated | 130.0 | 0.390 | 0.0001 | |
| FXL fit | 130.0 \pm 0.000 | 0.390 \pm 0.000 | N/A | -8.26 |
| NXL fit | 164.2 \pm 1.877 | 0.571 \pm 0.003 | N/A | -3.69 |
| 2PX fit | 130.2 \pm 0.030 | 0.391 \pm 0.000 | 0.001 \pm 0.000 | -6.47 |
| shutter-speed | 133.8 \pm 0.459 | 0.406 \pm 0.002 | 0.033 \pm 0.004 | -4.88 |
| NXL (8°) simulated | 130.0 | 0.390 | 1000 | |
| FXL fit | 89.8 \pm 0.934 | 0.238 \pm 0.002 | N/A | -3.64 |
| NXL fit | 130.0 \pm 0.001 | 0.390 \pm 0.000 | N/A | -8.43 |
| 2PX fit | 129.0 \pm 0.121 | 0.386 \pm 0.001 | 14.402 \pm 1.743 | -5.95 |
| shutter-speed | 124.6 \pm 0.159 | 0.374 \pm 0.001 | 0.392 \pm 0.001 | -5.62 |
| IX (8°) simulated | 130.0 | 0.390 | 0.5 | |
| FXL fit | 106.5 \pm 0.637 | 0.297 \pm 0.001 | N/A | -3.89 |
| NXL fit | 145.2 \pm 0.746 | 0.466 \pm 0.001 | N/A | -4.26 |
| 2PX fit | 130.8 \pm 0.133 | 0.395 \pm 0.001 | 0.548 \pm 0.007 | -5.76 |
| shutter-speed | 127.8 \pm 0.071 | 0.383 \pm 0.000 | 0.210 \pm 0.001 | -6.01 |

Table A2 – Example results of fits to simulated fibroadenoma data. Parameter values used to simulate the data are shown and below them parameter estimate \pm 95% confidence intervals from each model fit are shown. The best fit (according to the cAIC) is highlighted in bold.

| | $K^{trans} / \times 10^{-3} \text{ min}^{-1}$ | | v_e | | τ_1 / s | | cAIC |
|---------------------|---|-------------------------------|--------------|-------------------------------|---------------|---------------------------------|---------------|
| FXL (25°) simulated | 60.0 | | 0.620 | | 0.0001 | | |
| FXL fit | 60.0 | ± 0.001 | 0.620 | ± 0.000 | N/A | | -7.55 |
| NXL fit | 60.5 | ± 0.015 | 0.639 | ± 0.000 | N/A | | -6.17 |
| 2PX fit | 60.5 | ± 0.055 | 0.639 | ± 0.002 | 13.628 | ± 554.2 | -6.17 |
| shutter-speed | 60.7 | ± 0.068 | 0.952 | ± 0.002 | 0.621 | ± 0.005 | -5.82 |
| NXL (25°) simulated | 60.0 | | 0.620 | | 1000 | | |
| FXL fit | 59.4 | ± 0.015 | 0.600 | ± 0.000 | N/A | | -6.13 |
| NXL fit | 60.0 | ± 0.000 | 0.620 | ± 0.000 | N/A | | -11.85 |
| 2PX fit | 60.0 | ± 0.000 | 0.620 | ± 0.000 | 35.214 | ± 23.483 | -8.86 |
| shutter-speed | 60.3 | ± 0.060 | 0.946 | ± 0.001 | 0.628 | ± 0.004 | -5.92 |
| IX (25°) simulated | 60.0 | | 0.620 | | 0.5 | | |
| FXL fit | 59.5 | ± 0.014 | 0.601 | ± 0.000 | N/A | | -6.18 |
| NXL fit | 60.0 | ± 0.001 | 0.621 | ± 0.000 | N/A | | -7.69 |
| 2PX fit | 60.0 | ± 0.003 | 0.621 | ± 0.000 | 35.174 | ± 172.391 | -7.73 |
| shutter-speed | 60.4 | ± 0.060 | 0.947 | ± 0.001 | 0.627 | ± 0.004 | -5.92 |
| FXL (8°) simulated | 60.0 | | 0.620 | | 0.0001 | | |
| FXL fit | 60.0 | ± 0.000 | 0.620 | ± 0.000 | N/A | | -9.24 |
| NXL fit | 62.7 | ± 0.106 | 0.745 | ± 0.002 | N/A | | -4.87 |
| 2PX fit | 62.0 | ± 0.246 | 0.706 | ± 0.012 | 0.426 | ± 0.176 | -5.05 |
| shutter-speed | 60.7 | ± 0.066 | 0.950 | ± 0.002 | 0.616 | ± 0.005 | -5.50 |
| NXL (8°) simulated | 60.0 | | 0.620 | | 1000 | | |
| FXL fit | 55.6 | ± 0.115 | 0.482 | ± 0.002 | N/A | | -4.62 |
| NXL fit | 60.0 | ± 0.000 | 0.620 | ± 0.000 | N/A | | -9.63 |
| 2PX fit | 59.8 | ± 0.027 | 0.611 | ± 0.001 | 3.598 | ± 0.434 | -6.37 |
| shutter-speed | 60.2 | ± 0.069 | 0.745 | ± 0.031 | 0.445 | ± 0.045 | -5.31 |
| IX (8°) simulated | 60.0 | | 0.620 | | 0.5 | | |
| FXL fit | 57.3 | ± 0.074 | 0.528 | ± 0.002 | N/A | | -4.88 |
| NXL fit | 61.0 | ± 0.040 | 0.664 | ± 0.001 | N/A | | -5.46 |
| 2PX fit | 60.8 | ± 0.096 | 0.653 | ± 0.004 | 2.489 | ± 0.946 | -5.62 |
| shutter-speed | 60.8 | ± 0.286 | 0.826 | ± 0.031 | 0.487 | ± 0.049 | -5.09 |

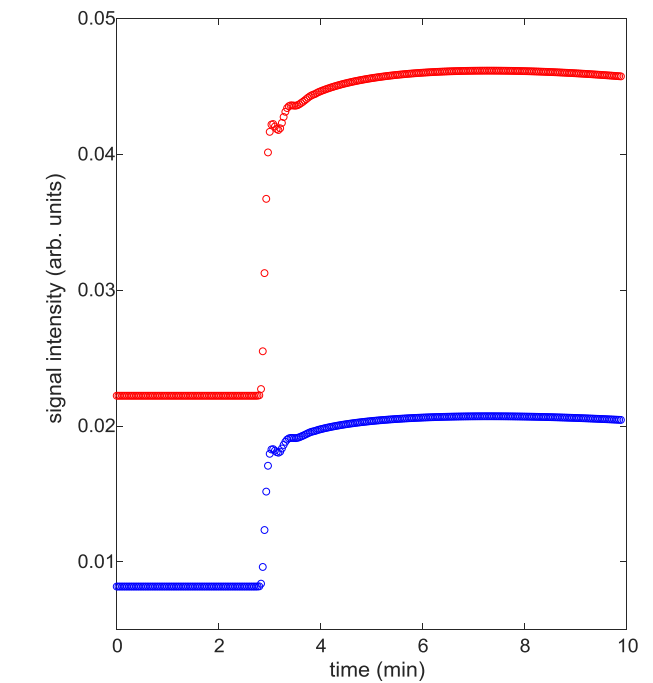
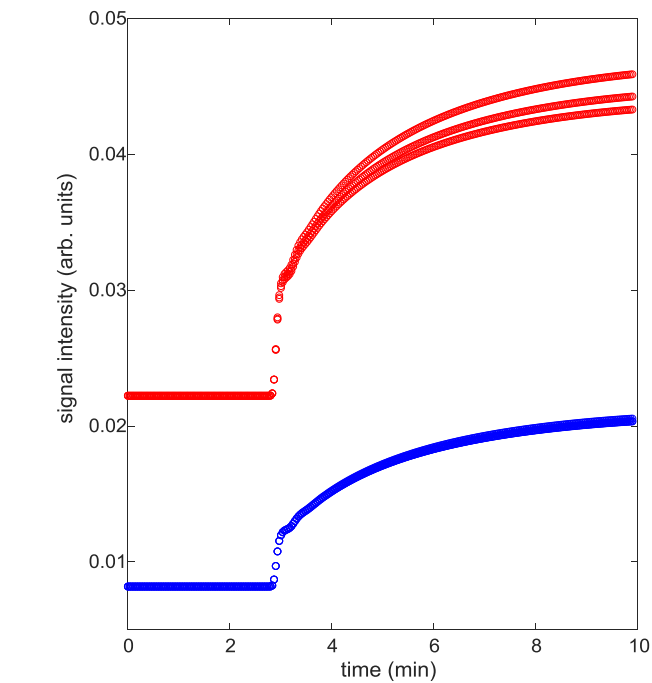
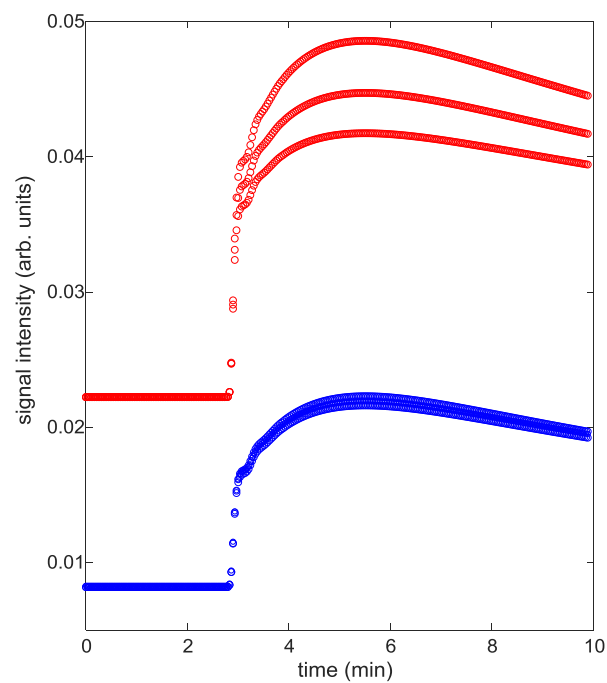


a



b

Fig. 1 – SI-time curves acquired from (a) the descending aorta of three different patients, (b) three malignant tumors (blue) and two benign fibroadenoma (red). Across the two plots the same symbols refer to data acquired from the same patients. The variable gap between the first set of baseline data and those acquired as the contrast agent arrives allows time for the acquisition of baseline high spatial resolution data and preparation of the patient for the injection.

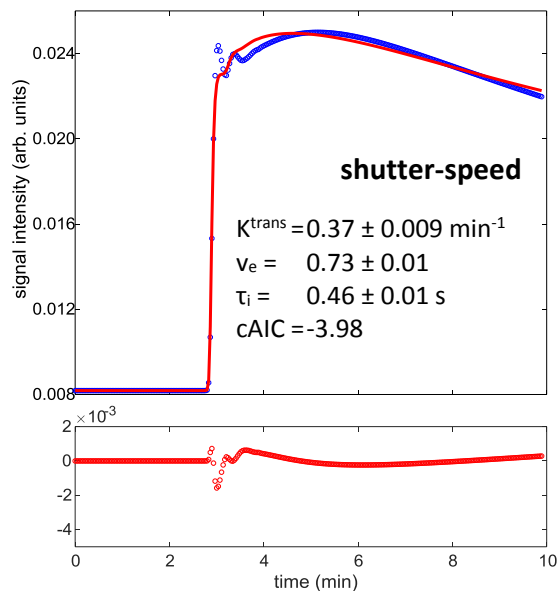
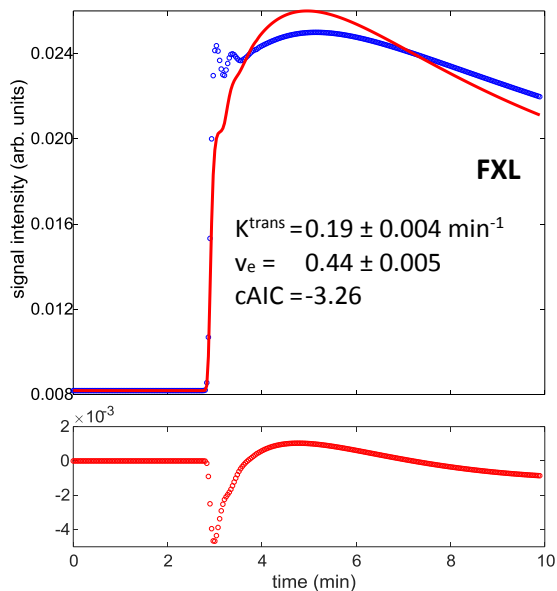


a

b

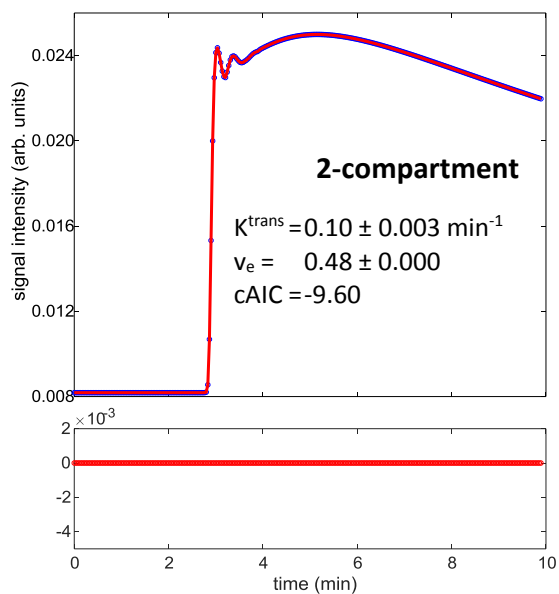
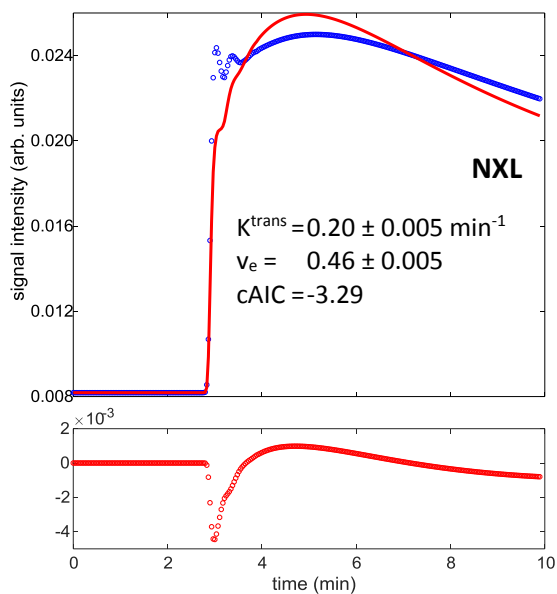
c

Fig. 2 - Simulated malignant (a & c) and benign data (b) using flip angles of 25° (blue) and 8° (red). Each flip angle was used to simulate data using a one-compartment tracer kinetic model with WX at the FXL, IX rate and NXL (a, b - top to bottom in each group, respectively). The data in (c) were simulated using a two-compartment tracer kinetic model and WX at the FXL.



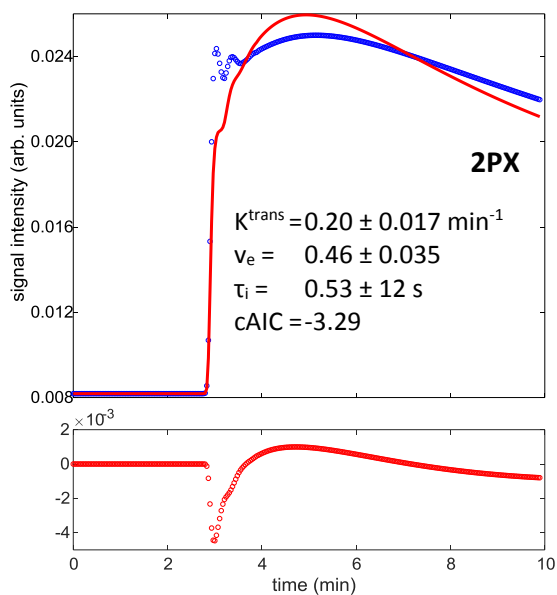
a

d



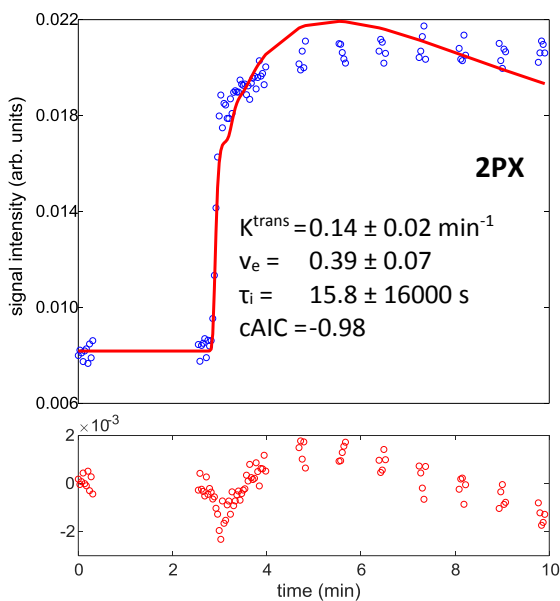
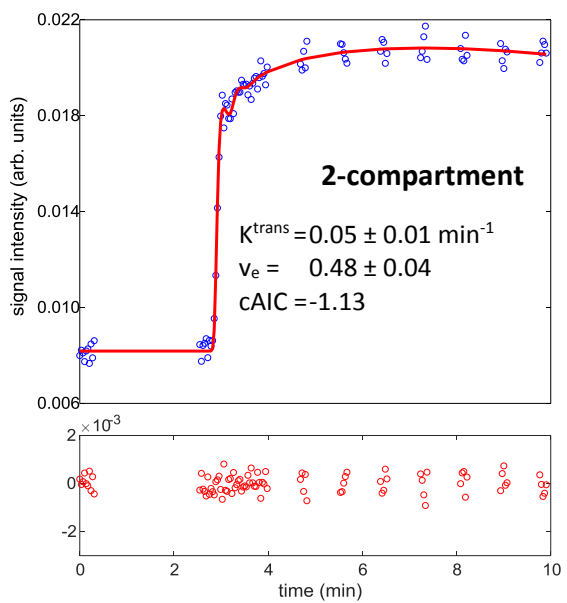
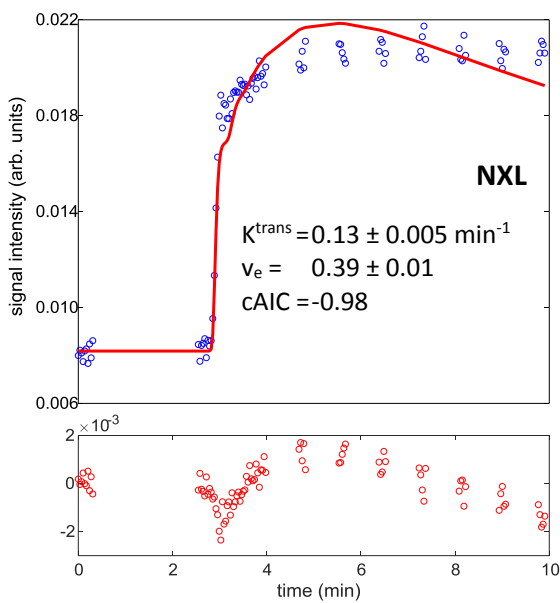
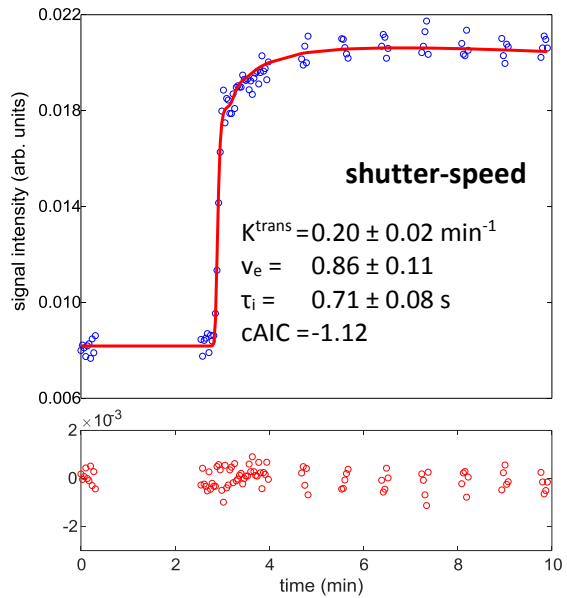
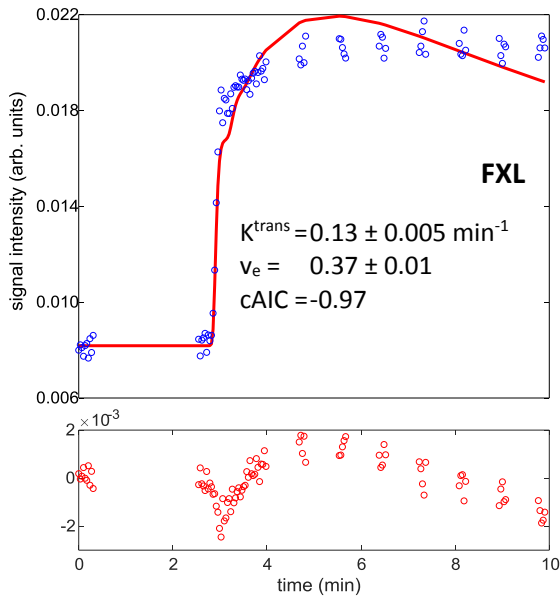
b

e



c

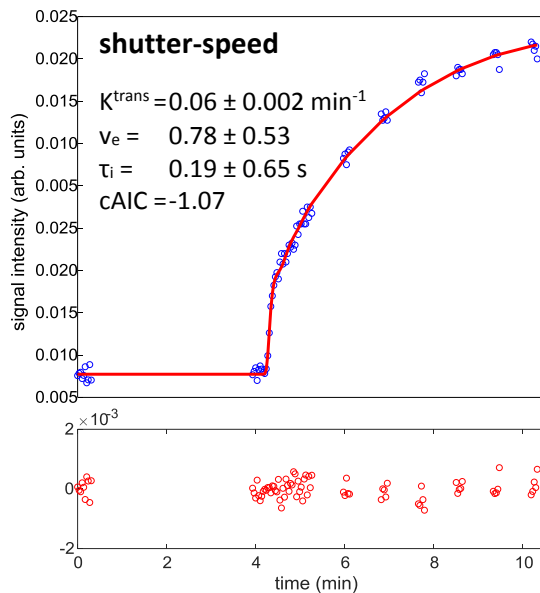
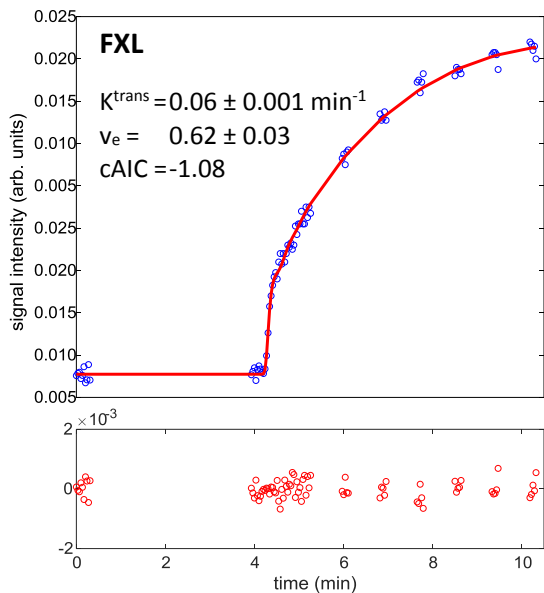
Fig. 3 - Model fits (red continuous lines) to one example simulated malignant tumor data set with WX at the FXL (blue circles). (a) FXL, (b) NXL, (c) 2PX, (d) shutter-speed and (e) two-compartment model (which produced parameter estimates exactly matching the simulation: $F_b = 0.50 \pm 0.00 \text{ ml} \cdot \text{min}^{-1} \cdot \text{ml}^{-1}$, $v_b = 0.27 \pm 0.00$, $PS = 0.16 \pm 0.00 \text{ ml} \cdot \text{min}^{-1} \cdot \text{ml}^{-1}$, $v_e = 0.32 \pm 0.00$). Each fit is accompanied by its parameter estimates, cAIC and (below) a plot of the fit residuals (red circles).



c

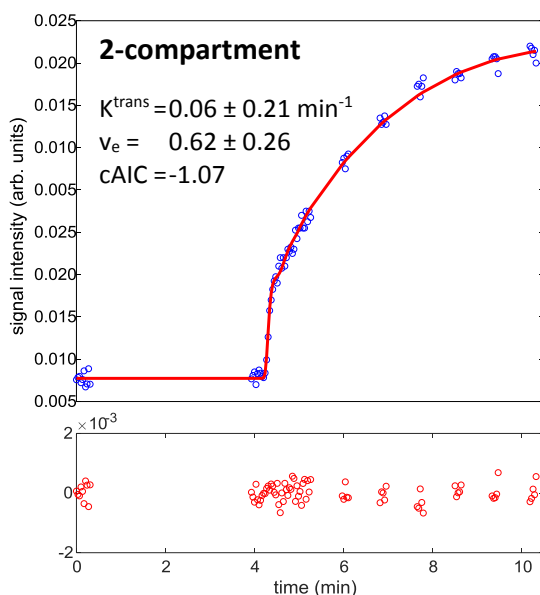
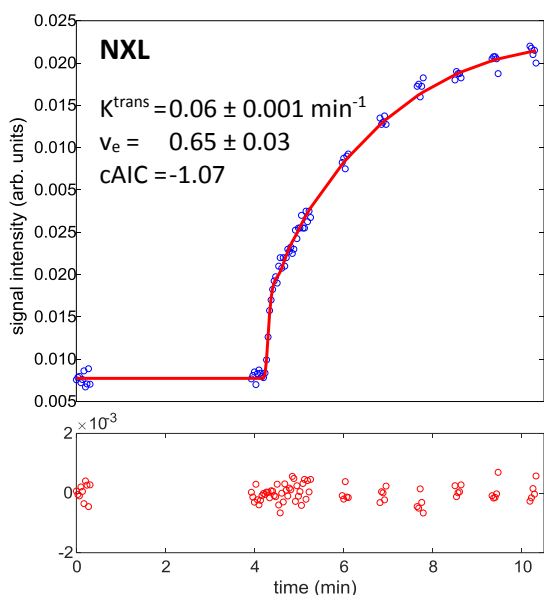
Fig. 4 - Model fits (red continuous lines) to clinical malignant tumor data from one example patient (blue circles). (a) FXL, (b) NXL, (c) 2PX, (d) shutter-speed and (e) two-compartment model (which produced the following parameter estimates: $F_b = 0.28 \pm 0.01 \text{ ml} \cdot \text{min}^{-1} \cdot \text{ml}^{-1}$, $v_b = 0.27 \pm 0.03$, $\text{PS} = 0.08 \pm 0.01 \text{ ml} \cdot \text{min}^{-1} \cdot \text{ml}^{-1}$, $v_e = 0.32 \pm 0.03$). Each fit is accompanied by its parameter estimates, cAIC and (below) a plot of the fit residuals (red circles).

c



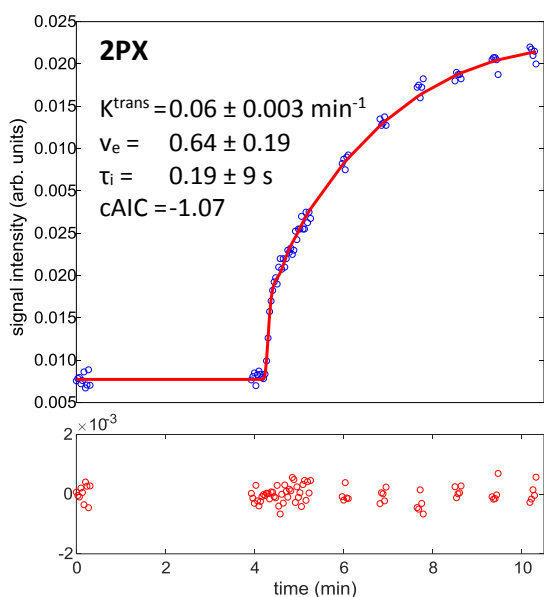
a

d



b

e



c

Fig. 5 - Model fits (red continuous lines) to fibroadenoma clinical data from one example patient (blue circles). (a) FXL, (b) NXL, (c) 2PX, (d) shutter-speed and (e) two-compartment model (which produced the following parameter estimates: $F_b = 0.11 \pm 0.06 \text{ ml} \cdot \text{min}^{-1} \cdot \text{ml}^{-1}$, $v_b = 0.04 \pm 0.30$, $PS = 0.43 \pm 1.34 \text{ ml} \cdot \text{min}^{-1} \cdot \text{ml}^{-1}$, $v_e = 0.59 \pm 0.18$). Each fit is accompanied by its parameter estimates, cAIC and (below) a plot of the fit residuals (red circles).

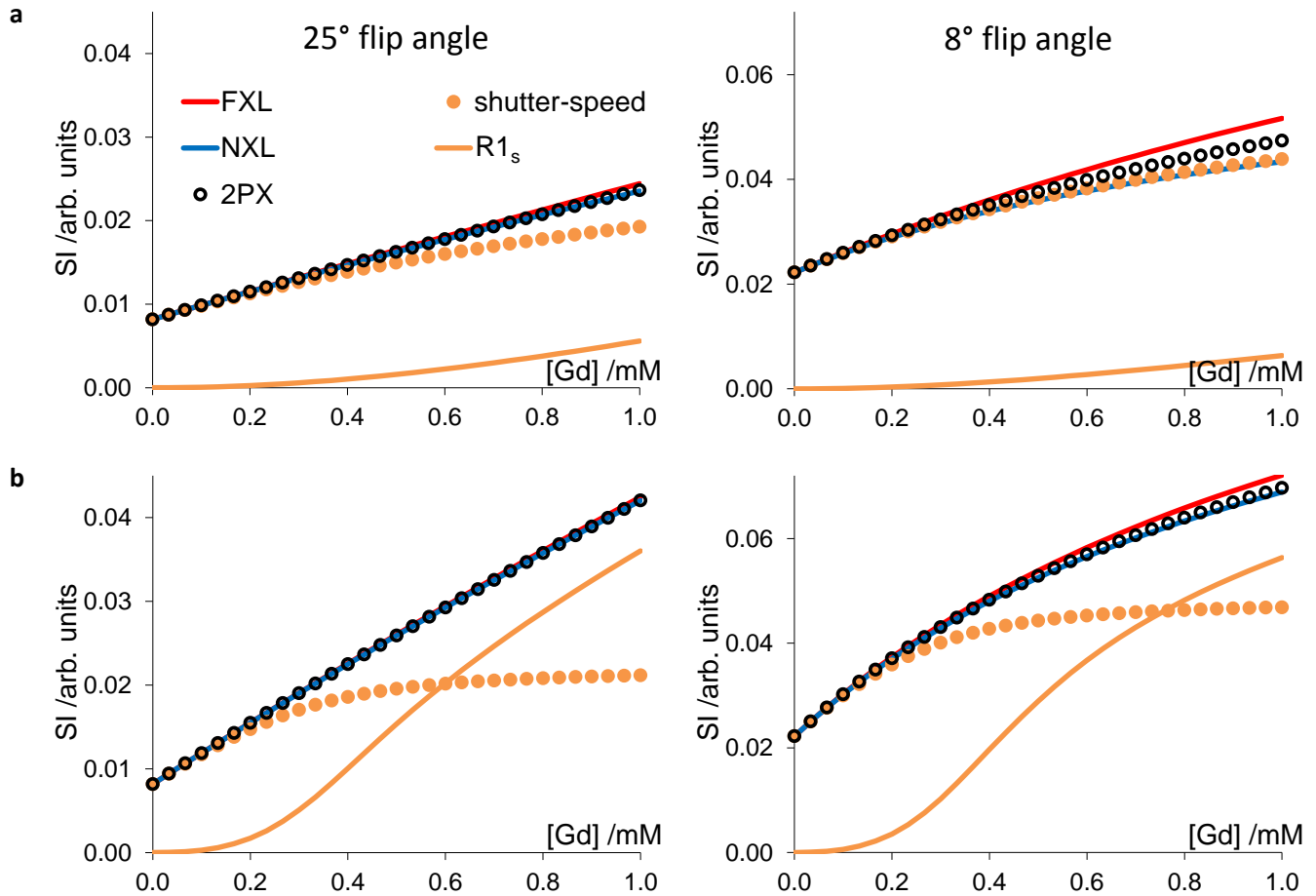


Fig. 6 – Calibration curves relating measured SI to interstitial concentration of contrast agent ([Gd]) using the sequence employed in this study (TR = 2.37 ms, flip angle = 25°, left column and 8°, right column) and a baseline T1 of 1282 ms. The calibration curves largely overlap for the FXL, NXL and 2PX models at 25°. The mismatch between the shutter-speed calibration curves and those of the 2PX can be explained by the missing $R1_s$ component that is additionally shown in these plots. (a) malignant tumor calibration curves calculated with a v_e of 0.39 and τ_i of 400 ms, (b) malignant tumor with v_e of 0.86 and τ_i of 714 ms.